

Seismic interferometry by tangent-phase correction

Flavio Poletto^{1*}, Biancamaria Farina¹, Gualtiero Böhm¹ and Kees Wapenaar²

¹OGS (Istituto Nazionale di Oceanografia e di Geofisica Sperimentale), Borgo Grotta Gigante 42c, 34010 Sgonico, Trieste, Italy, and ²Department of Geoscience and Engineering, Delft University of Technology, 2600 GA Delft, The Netherlands

Received April 2013, revision accepted August 2014

ABSTRACT

We present a modified interferometry method based on local tangent-phase analysis, which corrects the cross-correlated data before summation. The approach makes it possible to synthesize virtual signals usually vanishing in the conventional seismic interferometry summation. For a given pair of receivers and a set of different source positions, a plurality of virtual traces is obtained at new stationary projected points located along the signal wavefronts passing through the real reference receiver. The position of the projected points is estimated by minimizing travel times using wavefront constraint and correlation-signal tangent information. The method uses mixed processing, which is partially based on velocity-model knowledge and on data-based blind interferometry. The approach can be used for selected events, including reflections with different stationary conditions and projected points with respect to those of the direct arrivals, to extend the interferometry representation in seismic exploration data where conventional illumination coverage is not sufficient to obtain the stationary-phase condition. We discuss possible applications in crosswell geometry with a velocity anomaly and a time lapse.

Key words: Seismic interferometry, Stationarity, Tangent, Phase, Wavefield.

1 INTRODUCTION

Seismic interferometry (SI) is the known process of cross-correlating and subsequently summing the cross-correlations of seismic traces recorded at different locations. This method makes it possible to recover virtual signals as if seismic sources were used in the receivers position (e.g., Bakulin and Calvert 2006; Wapenaar and Fokkema 2006; Schuster 2009). In the conventional seismic interferometry approach by cross-correlation (or equivalently its variant by deconvolution), the virtual signals can be properly recovered provided that the coverage by real sources illuminating the receivers is realized in a way that stationarity conditions are obtained for the reconstructed wavefields (Snieder 2004). An issue in the standard method application lies in the fact that, in several seismic exploration geometries, as well as in passive seismic applications, in practice only partial coverage by real sources

may be available for the virtual signals we wish to recover. With insufficient coverage, the interferometry results are distorted or vanish. The method discussed in this paper uses a modified processing approach (Poletto, Farina, and Böhm, 2012b), which makes it possible to overcome the limitation for the conventional stationarity condition, and to extend the interferometry representation for selected events beyond the natural Fresnel zone (Spetzler and Snieder 2004).

This study relates to a generalized-phase interferometry (GPI) method based on tangent analysis, which corrects the cross-correlation data before making the summation to get the estimate of the Green's function by Kirchhoff–Helmholtz wavefield representation. The methodology, which uses a linear approach similar to Radon transforming in the cross-correlation domain for imaging purposes (Miller, Oristaglio, and Beylkin 1987) allows us to synthesize virtual signals usually vanishing in the conventional seismic interferometry summation. The modified approach involves a remapping of the representation points where new virtual sources are redatumed,

*E-mail: fpoletto@ogs.trieste.it

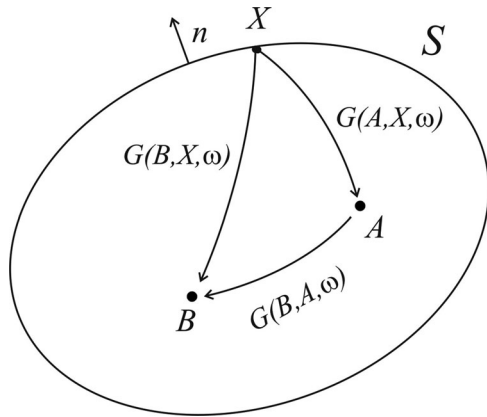


Figure 1 Classical representation for seismic interferometry with receivers in A and B completely surrounded by sources at X on the encompassing surface S. The small arrow indicates the outward normal n to the surface.

thus moving the position of the new virtual sources away from that of the standard virtual source at a receiver. For a given pair of receivers, new traces are obtained at new stationary projected points for different source locations along the signal wavefronts passing through the real reference receiver. The process of generalized reconstruction involves the identification of these points. We appraise the position of the projected points minimizing the travel times by the constraint that the points are on the signal wavefronts and making use of the tangent information. The approach, which uses mixed processing partially based on velocity-model knowledge and on data-driven interferometry without the need of knowing the local velocity model, is adopted and demonstrated for selected events. Different events, such as direct arrivals and reflections, have different stationary conditions and projected points. The method makes it possible to use interferometry with seismic exploration data when conventional illumination coverage is poor and inadequate to provide stationary-phase conditions.

1.1 Seismic interferometry conventional representation

To introduce the modified representation approach, we start from the integral representation typically used for conventional seismic interferometry with the simple model geometry of Fig. 1. We assume real unknown seismic sources at points X distributed over the source domain S, and surrounding two receivers located in A and B. The acoustic medium is arbitrary. It is well known that when the encompassing sources completely surround the receivers, this configuration represents the ideal condition of complete coverage for the

recovery of the Green's function $G(B, A)$ between the points A and B. For convenience, we revisit the interferometry correlation derivation expressed in the Fourier frequency domain by the acoustic reciprocity theorem of correlation type (Wapenaar and Fokkema 2006)

$$G^*(B, A, \omega) + G(A, B, \omega) = \frac{i}{\omega\rho} \int_S \left[\frac{\partial G(B, X, \omega)}{\partial n} G^*(A, X, \omega) - \frac{\partial G^*(A, X, \omega)}{\partial n} G(B, X, \omega) \right] dS, \quad (1)$$

where the integration is extended over the source domain S, ω and ρ are the angular frequency and mass density, respectively, $i = \sqrt{-1}$, and the symbol * denotes complex conjugation. Equation (1) provides the exact representation of the Green's function and its reciprocal between receivers A and B when the propagating wavefields from the surface sources are known at these receivers, together with the wavefields from surface dipole sources. These are expressed by functions with dipole character given by the normal derivative of the wavefields at the surface S. In common practice, the high-frequency normal derivative $\partial/\partial n = (-i\omega/c)\cos\gamma$, where c is the propagation velocity and γ is the angle between the pertinent ray and the normal to the surface, is often approximated as $\partial/\partial n = -i\omega/c$, simply assuming normal incidence (Wapenaar and Fokkema 2006). Furthermore, invoking source–receiver reciprocity and observing that the main contributions in (1) come from the stationary points on S (e.g., Schuster 2009) provide the simplified formulation of equation (1) frequently used for the interferometry representation. This leads to rewriting the cross-correlation integral representation of seismic interferometry, that provides the familiar estimate of the Green's function $G(B, A, \omega)$ between the points A and B as

$$G^*(A, B, \omega) + G(B, A, \omega) \cong \int_S G(B, X, \omega) G^*(A, X, \omega) dS. \quad (2)$$

Here, the symbol of equivalence is used to mean that the reconstruction of the Green's function at the left-hand side of equation (2) is given by the term at the right-hand side apart from a scaled time derivative that expresses a dipole response operator. The Green's function may assume different forms depending on the type of representation for the wavefields by Green's functions. Note that equation (2) gives only one trace in the frequency domain. This provides two virtual seismic signals when stationary-phase conditions with complete illumination from real sources disposed around receivers are satisfied. One signal is the causal part of $G(B, A, t)$, i.e., the time signal obtained by

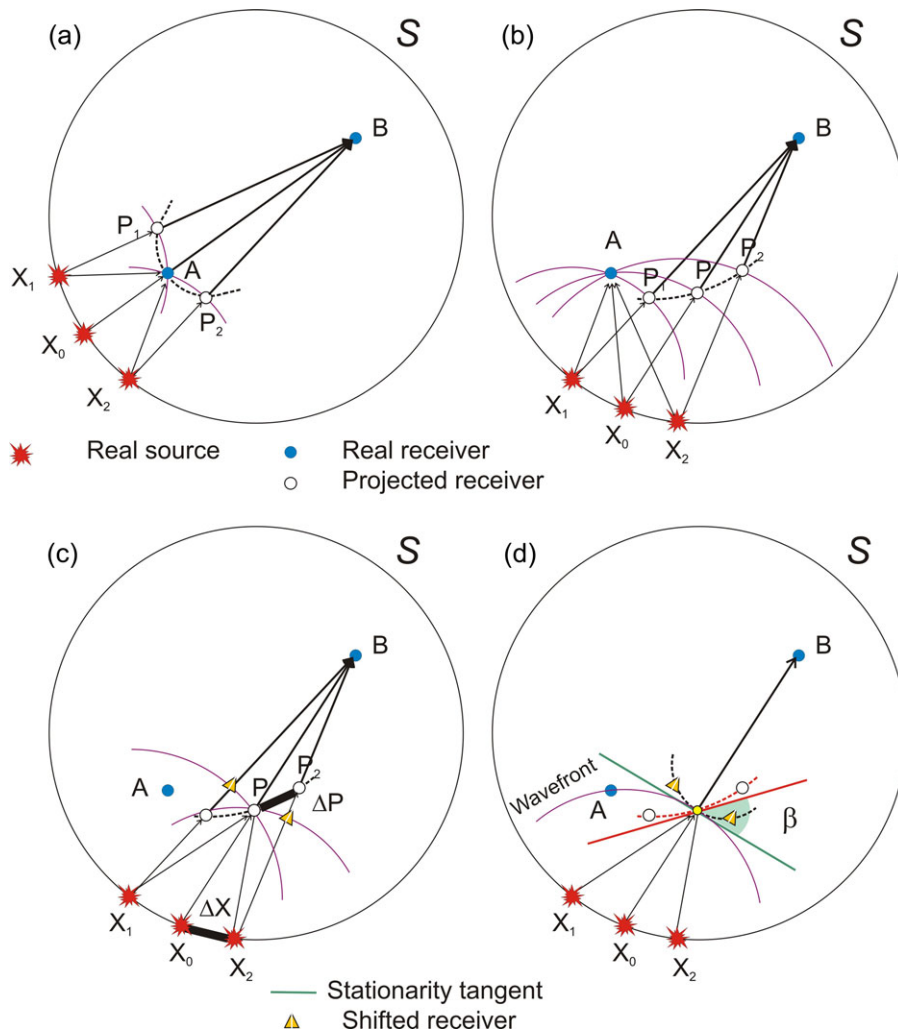


Figure 2 (a) The region around the real source X_0 is stationary for seismic interferometry in the conventional sense. The projected receiver points P_1 and P_2 are located intersecting the wavefronts generated in X_1 and X_2 and passing in A with the rays from these sources to B . These points are on a path (black dashed line) with a stationary point in A . (b) The source X_0 is in a non-stationary region. The projected points are on a slanted non-stationary curve in P . (c) Triangles represent the shifted projected points on stationary positions around P . Bold lines represent small increments ΔX and ΔP of the source and of the projected point, respectively. (d) The angle β between the tangents to the wavefront in P and to the non-stationary slanted path of the projected points (red dashed line) is used to shift the points to the stationary (black dashed) path.

inverse Fourier transforming $G(B, A, \omega)$ that furnishes the Green's function from A to B ; and the other signal is the anti-causal part of the time reversal $G(A, B, -t)$ of the Green's function from B to A obtained by inverse Fourier transforming $G^*(B, A, \omega)$. We remark that, by invoking source–receiver reciprocity, we have $G(B, A, t) = G(A, B, t)$.

An important limitation in the process of natural data redatuming (Schuster and Zhou 2006) by conventional seismic interferometry is that the illumination coverage by real sources may not be sufficient in practice, so that the conventional virtual results may be distorted, e.g., when we deal only

with illumination from source regions outside of the required conventional stationary regions. In this work, we present a generalized method based on tangent-phase correction for improving the coverage and the seismic illumination for geophysical exploration purposes. This approach is not defined as global because it is suited and intended for selected events. For selected events, the stationary-phase conditions are extended to lateral positions beyond the region around the real sources where the conventional stationarity condition is satisfied (Snieder 2004; Poliannikov and Malcolm 2011). Consequently we obtain new projected virtual sources,

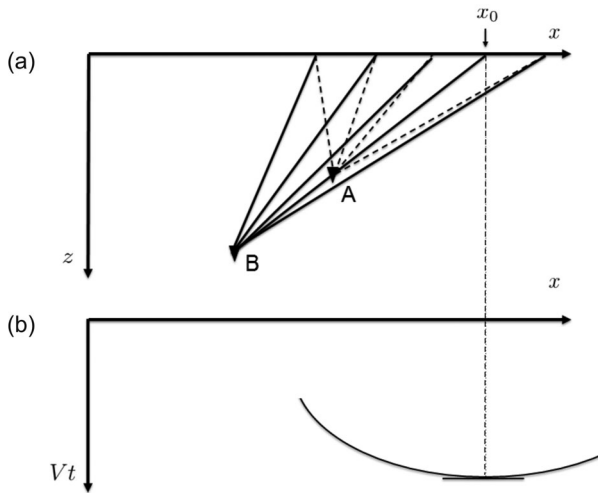


Figure 3 Stationary interferometry condition in the seismic exploration geometry. (a) shows the (x, z) space model, where x is the surface source coordinate and A and B are receivers. Assuming a medium of uniform velocity V , the source at stationary position x_0 in (a) corresponds in the (x, Vt) model (b) to a flat tangent to the curve of the cross-correlations between signals recorded in A and B .

say, at ideal receivers migrated laterally. Conventional interferometry uses natural, i.e., data based, information and does not need model information. The proposed generalized-phase interferometry (GPI) approach uses both natural and model-based information to estimate the Kirchhoff–Helmholtz representation at the new projected virtual points. We denote this generalized method based on tangent-phase correction as tangent-phase interferometry TPI.

2 TANGENT-PHASE APPROACH: A THEORY

To introduce the concept, we consider the simple case of Fig. 2, where the signals are generated by sources located on a circle S enclosing two receivers positioned in A and B . We assume a uniform medium and analyze the propagation of the direct arrivals (i.e., selected events). Figure 2a represents a real source X_0 in a stationary-phase region, i.e., including the Fresnel zone, on S for the interferometry representation of virtual signals from A to B . This condition can easily be verified by signal cross-correlation analysis, and it can be examined also graphically by observing the composition of the corresponding ray paths and wavefronts. The graphical approach helps us to introduce and discuss the generalized representation around X_0 . We start from the stationary case of panel in Fig. 2a. We consider here for simplicity only two sources

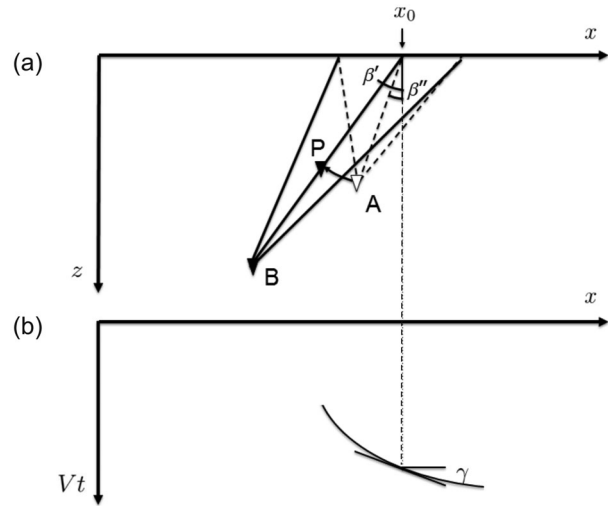


Figure 4 Non-stationary interferometry condition for the source in x_0 in the space model (a). In this case, the tangent to the curve in x_0 is not flat in the (x, Vt) model (b). To obtain stationarity, the receiver in A is moved to the projected point P on the wavefront. Equation (10) relates γ and the angles β'' and β' for A and P in (a). The non-stationary tangent angle γ is related to the apparent angle of the tangent to the cross-correlations in the (x, t) domain by Equation (12).

X_1 and X_2 located laterally with respect to X_0 . Considering the approach from the standpoint that the method corrects the travel times neglecting amplitude in the interferometry representation, the wavefront of a signal from X to A can be defined as the locus of all the points P that satisfy the condition

$$G(P, X, \omega) = G(A, X, \omega), \tag{3}$$

in the Fourier frequency domain. Since, in the following, we assume partial knowledge of the model and knowledge of the sources, in principle, further careful analysis could be done to include and compensate also for amplitude variations in the Green’s function (Vinje, Iversen, and Gjoystdal 1993) as well as for source’s directional balancing (Curtis and Halliday 2010). If we intersect the wavefronts of the signals generated in X_1 and X_2 and passing in A with the rays from these sources to B , we locate the projected receiver points P_1 and P_2 . The point P_i ($i = 1, 2$) represents a virtual receiver on the raypath from the source X_i to B . By construction, the cross-correlation of the signal recorded in P_i with the signal recorded in B equals the cross-correlation of the signal recorded in A with the signal recorded in B from X_i . The radial distance from B to the curve of projected receiver points (P_1, A, P_2) represents graphically the cross-correlation delay, showing a trend with the local

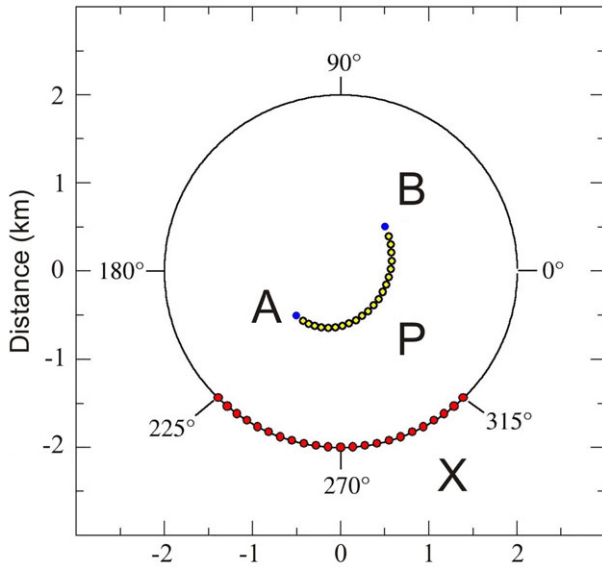


Figure 5 Synthetic example with a circle of sources in a uniform medium. Model with the projected points (P) for a selected section of sources (X).

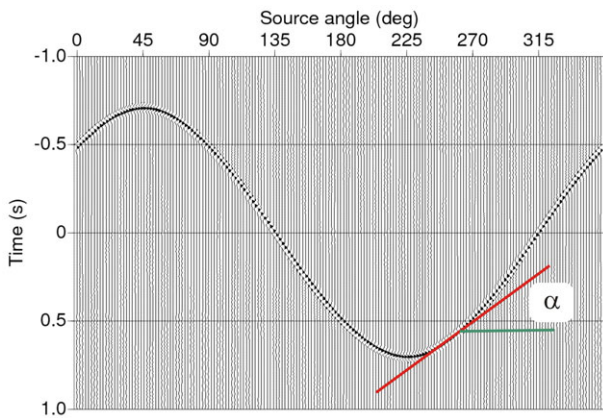


Figure 6 Synthetic example with a circle of sources in a uniform medium. Cross-correlations between signals recorded in A and B. The tangent line (red line) and the corresponding apparent angle are shown for the source at the reference position 260° .

maximum at A, i.e., the stationary cross-correlation time before interferometry integration. This trend is shown here only for three points, but it is representative for the sources densely sampled on S in the region around X_0 to prevent from aliasing effects.

Now we move away from the source stationarity region. It is evident that, if we shift laterally the position of the reference source X_0 as in Fig. 2b, the curve of the projected points (P_1, P, P_2) no longer has a stationary point; therefore, the conventional integration vanishes in this zone, as expected. In this

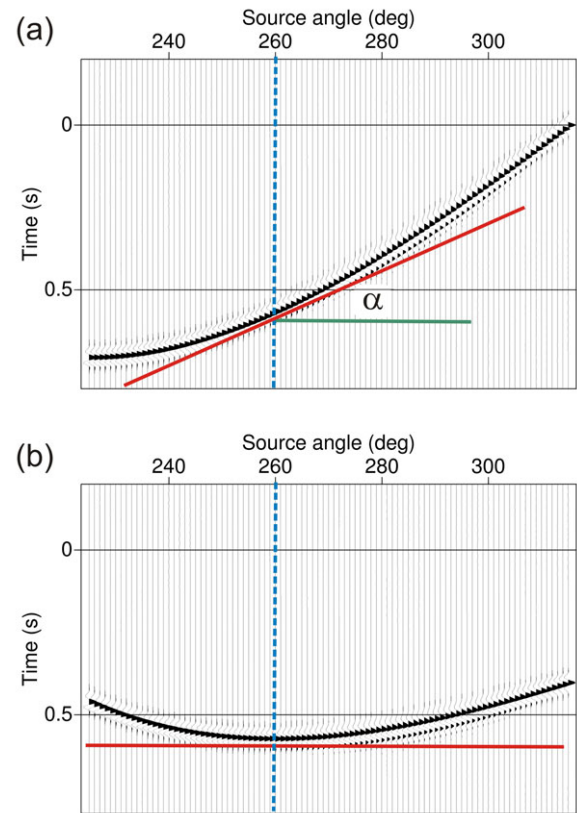


Figure 7 Cross-Correlated data before stack, (a) before and (b) after correction of the tangent for the point at source angle 260° (dashed blue line).

case the central point of the projected region is the projected point P but without a virtual signal converging in the conventional interferometry representation. In order to have the simulation of a new-ideal real receiver at P, we need a stationary condition for the signals from the sources illuminating P, similar as for those signals from the sources illuminating A. To obtain this result in relation to B, we need to find the shifted projected points (represented by triangles in Fig. 2c) to reproduce stationary condition as in Fig. 2a. They are given (Fig. 2c) by the intersection of the wavefronts generated by the shifted sources X_1 and X_2 and passing in P with the rays from these sources to B. To solve this problem, we use a generalized approach based on an analysis of the tangent stationarity phase. If we assume that the variation is local, i.e., the variation in the remaining part of the paths between P and B is negligible, the solution is achieved in a first-order approximation by correcting the phase corresponding to the slope given by the angle $\beta = \beta(A, B, X_0)$ (Fig. 2d). This is the angle between the tangent to the envelope of the projected receiver curve (red

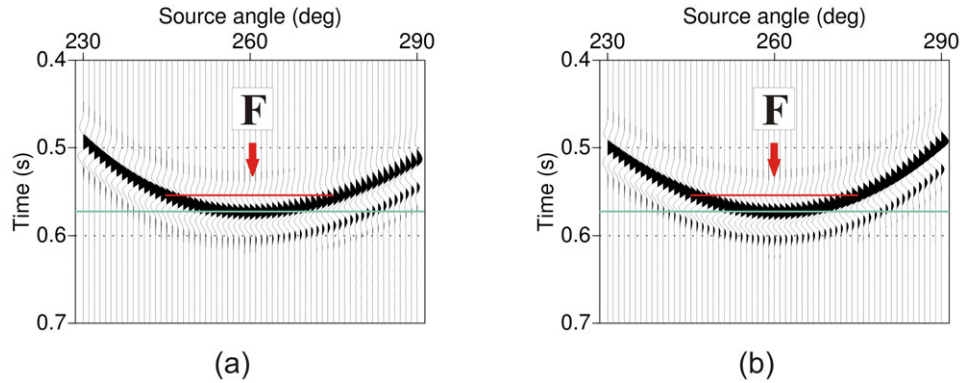


Figure 8 Comparison of Fresnel zones (F) in the interferometry signals before stack of the cross-correlations. The signals are calculated for the point at the source angle 260° . (a) TPI stationary signal after tangent-phase correction. (b) Conventional interferometry signal calculated using the corresponding projected point $P(260)$ to record the signals of the sources on the circle for cross-correlation with the signal recorded in B. This signal is stationary for construction. The TPI Fresnel zone calculated by a first-order approximation is similar to the Fresnel zone of the conventional interferometry representation.

line) and the tangent in P to the wavefront of the signal from X_0 (green line) (or that of the signal from B to P —here we assume that these wavefronts have the same tangent in P). The black-dashed line (Fig. 2d) evidences the shifted curve passing through the triangles, which is stationary, as in Fig. 2a.

2.1 Model-based approach

This analysis leads to a modified representation integral for the specific source at the reference point X_0 given by

$$G(B, P, \omega) \cong \int_{S_0} G(B, X, \omega) G^*(A, X, \omega) C(\beta, V, X, X_0, \omega) dS, \quad (4)$$

where $P = P(A, B, X_0)$ is the projected receiver point associated to X_0 (here we assume uniqueness of the projected point for simplicity), V is the medium velocity, and S_0 represents a finite part of the integration surface, according to the fact that we only show the causal function G on the left-hand side of equation (4). The term

$$C = C(\beta, V, X, X_0, \omega) \quad (5)$$

is a phase-shift operator applied to the cross-correlations and include a slope correction with zero shift in $X = X_0$. Using equation (3), we can reformulate equation (4) as

$$G(B, P, \omega) \cong \int_{S_0} G(B, X, \omega) G_0^*(P, X, \omega) dS, \quad (6)$$

where

$$G_0(P, X, \omega) = G(P, X, \omega) C^*(\beta, V, X, X_0, \omega), \quad (7)$$

can be interpreted as the shifted Green's function achieved using the phase-shift operator C for X_0 . We underline the fact

that the application of this approach using only two receivers (e.g., A and B) produces a multiplicity of new traces after integration, whereas the conventional Equation (2) provides only one trace (here we limit the integration domain on S_0 and neglect the discussion about causal and anticausal representation by reciprocity). For each selected event (in our examples the direct arrival), a new TPI virtual signal can be obtained for each real source X_0 by correcting the slope for the illumination from a suitable region around X_0 . The representation of another event (e.g., a reflection), different from the selected one for the correction analysis, in general does not converge with the same slope, even if it may do in particular cases of common travel paths.

2.2 Data-based approach

The tangent analysis to get the correction can be performed on signals in the cross-correlation time domain before integration. Obviously, the apparent angle determined from tangent analysis for the correction of the correlated signal in the source domain is related to the data representation in the space domain. Consider a small shift ΔX of the source with respect to the reference source position X_0 on the surface S , and the resulting increment ΔP of the projected point position (see Fig. 2c, where the increments are represented by bold lines). The radial increment related to ΔP can be approximated as

$$\Delta R = V \Delta t = \Delta P \sin \beta, \quad (8)$$

where Δt is the correlation time increment, and β is the angle between ΔP and the wavefront tangent in P . Using the angle β to determine Δt needs the knowledge of V and ΔP .

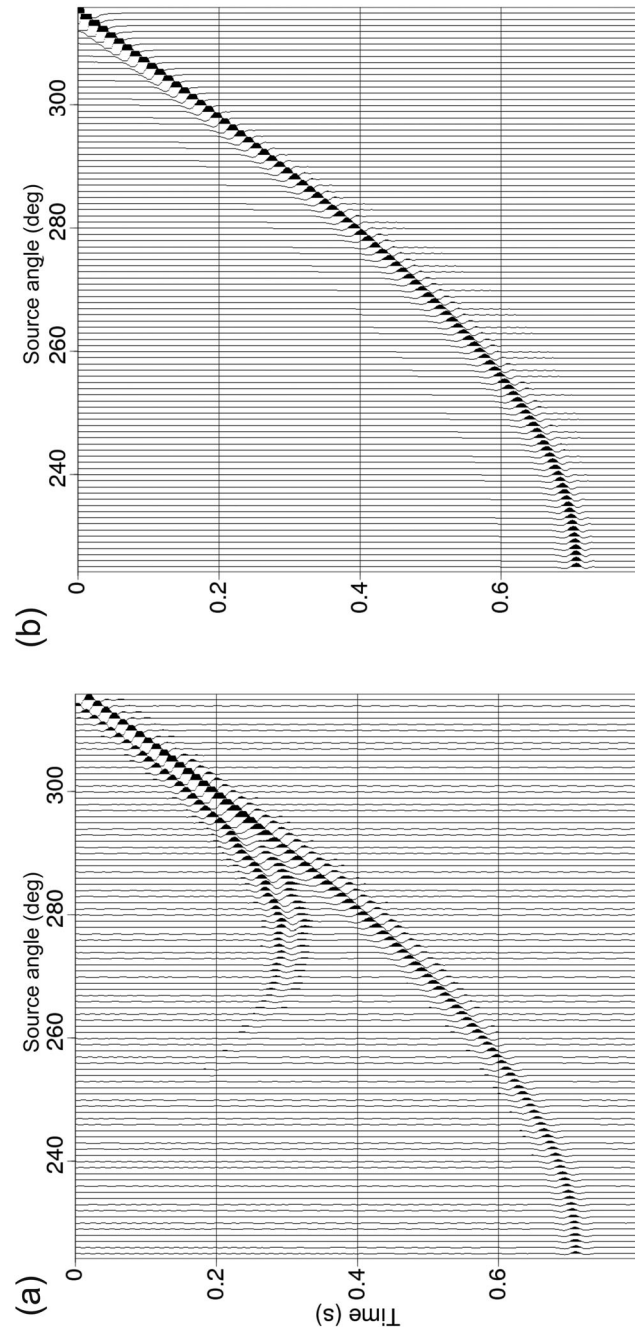


Figure 9 In (a) the data are stacked after tangent correction for source angles between 225° and 315°. For comparison, (b) shows signals recorded at receiver B with acoustic sources simulated at the corresponding projected points.

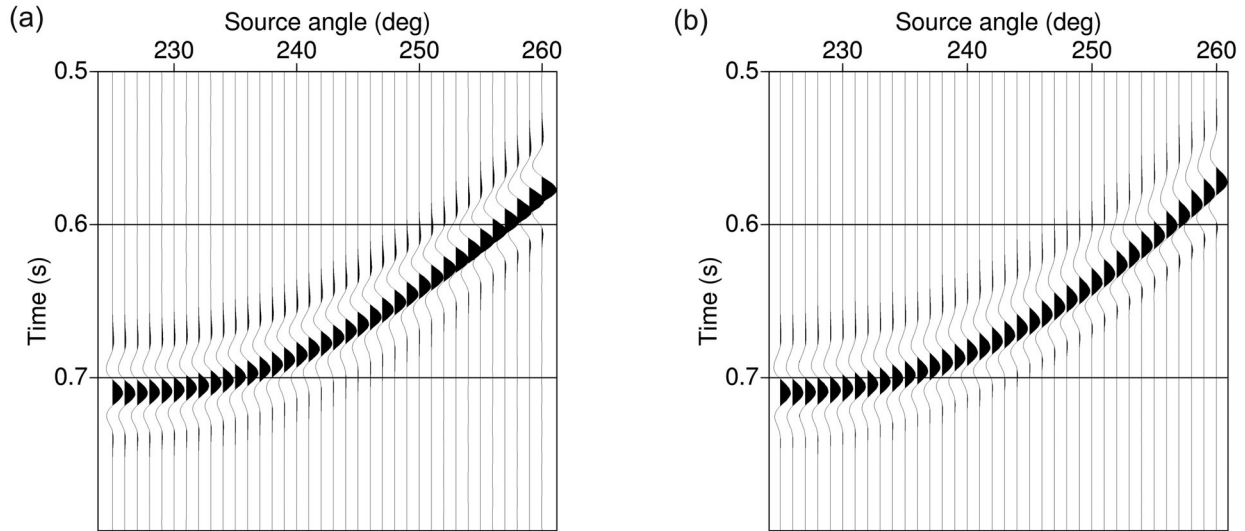


Figure 10 Detail of Fig. 9(a,b), in which we compare (a) generalized-phase interferometry results and (b) corresponding synthetic signals.

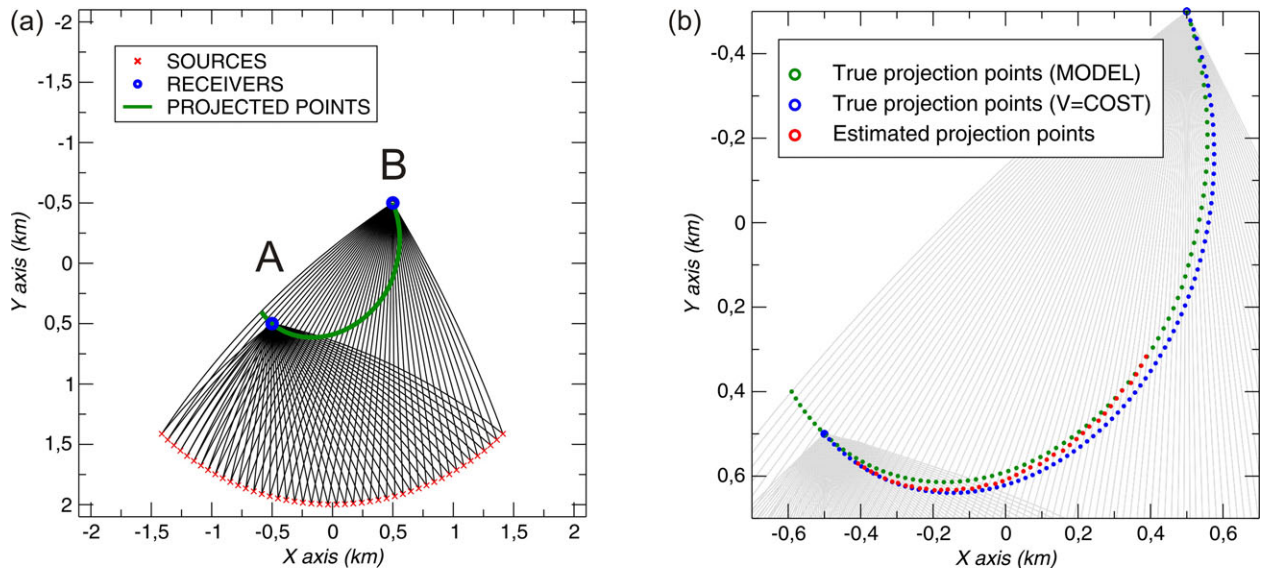


Figure 11 (a) The TPI points P in the variable model. (b) Calculated positions of the points in a variable model (vertical velocity gradient) up to the limit of the known model (first iteration step).

In practice, we use a data-based approach picking the cross-correlations of selected events, which does not require model information to estimate the shift in the first-order approximation. With respect to the model-based approach, which can be applied estimating β and using the local velocity V , the data-based approach has the difference that it includes all the delays through the paths from P to B. If we assume as relevant only local effects, the apparent-tangent angle α given by the generalized stationary-phase analysis, i.e., picking the time delay in the cross-correlation data represented in the source domain

and calculating the local tangent, is related to the space angle β by

$$\alpha = \tan^{-1} \frac{\Delta t}{\Delta X} = \tan^{-1} \left[\frac{\Delta P \sin \beta}{\Delta X V} \right], \quad (9)$$

where ΔX is known from the source geometry in exploration data. We assume that the source is represented in a first-order approximation in a domain related to the source spatial coordinate by a suitable linear relationship. The TPI method determines the position of the projected virtual receivers

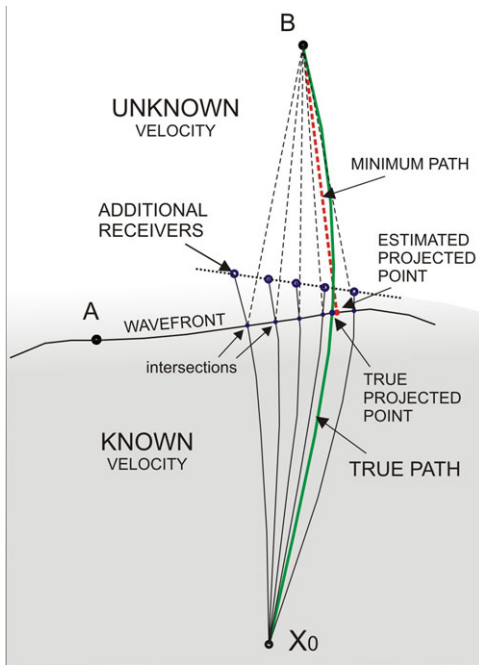


Figure 12 A projected point is located by traveltime minimization using the known model properties and the data tangent. To estimate the wavefront, a set of fictitious additional receivers was used in the known velocity model including the wavefront.

associated to the TPI signals requiring that the projected points belong to the wavefronts passing through the reference receiver, which in this case is A. We use ΔP in equations (8) and (9) and the partial knowledge of the model inside the representation domain for the estimation of the tangent angle β . Figures 3 and 4 illustrate a simple representation of the same concepts in the seismic exploration geometry. Here x is the horizontal coordinate, and Vt is the vertical one, used for convenience to obtain dimensionless angles in the Cartesian domain (x, Vt) . In this case an equivalent projection analysis by angles is expressed at the position x_0 of the source, and not only at the projected point P. In a uniform medium, the following relationships with equations (8) and (9) hold for the non-stationary tangent angle γ (Fig. 4)

$$\tan \gamma = \sin \beta' - \sin \beta'', \quad (10)$$

$$\frac{\Delta P}{\Delta x} = \frac{\sin \beta' - \sin \beta''}{\sin \beta}, \quad (11)$$

$$\tan \alpha = \frac{1}{V} \tan \gamma, \quad (12)$$

where β' and β'' are the angles of P and A with respect to the vertical axis in x_0 . In arbitrary media, a model-based analysis

is needed to relate the angles at x_0 to α and to the projected points and β .

The apparent angle α calculated from the data is used in the correlation-time versus source-space domain and can have different dimensions, depending on the type of representation used for the source space X . The phase-shift operator applied to the correlation function in the integrand of Equation (4) (or to the Green's function of Eq. 7) for obtaining stationarity in a region centred around the reference source X_0 can be expressed as

$$C_d(\alpha_0, X, X_0, \omega) = (i\omega/V)e^{-i\omega \tan(\alpha_0)(X-X_0)} \quad (13)$$

where $\alpha_0 = \alpha(X_0)$. Substituting in equation (4) gives

$$G(B, P, \omega) \cong (i\omega/V) \int_{S_0} G(B, X, \omega) G^*(A, X, \omega) e^{-i\omega \tan(\alpha_0)(X-X_0)} dS. \quad (14)$$

We may observe the analogy between this approach and a τ - p transform performing slanted stack with time origin in X_0 (e.g., Stoffa 1989). Equation (13) corrects the slope of the correlation function in the integrand of the right-hand side term of equation (4) in such a way that its first derivative vanishes and we reconstruct a simple stationary point in X_0 (Bleistein 1984, pp. 77) for selected events. The subscript 'd' denotes that we have included in the operator (13) the dipole character represented – neglecting amplitude effects – by the operator $(i\omega/V)$ calculated in the normal-incidence approximation with respect to the surface S as discussed for equation (1).

3 EXAMPLES AND PROCESSING

3.1 Uniform acoustic model

We consider the explicative example of a 2D acoustic model with uniform velocity of 2 km/s and a set of seismic sources, distributed on a circle with a radius of 2 km and spaced 1° in polar coordinates. These coordinates are used for convenience in place of X to represent the sources in this geometry (Fig. 5). The model is discretized by square pixels of 5 m side. We focus the analysis for the projected signals in the source-angle range from 225° and 315° (red dots). Two receivers, A and B, are placed at Cartesian coordinates $(-0.5, -0.5)$ km and $(0.5, 0.5)$ km, symmetrically with respect to the centre of the model. Transient synthetic signals are generated at each source position on the circle and recorded in A and B. The wavefields were calculated by a finite-difference code. The average and cutoff frequencies of the source wavelet are

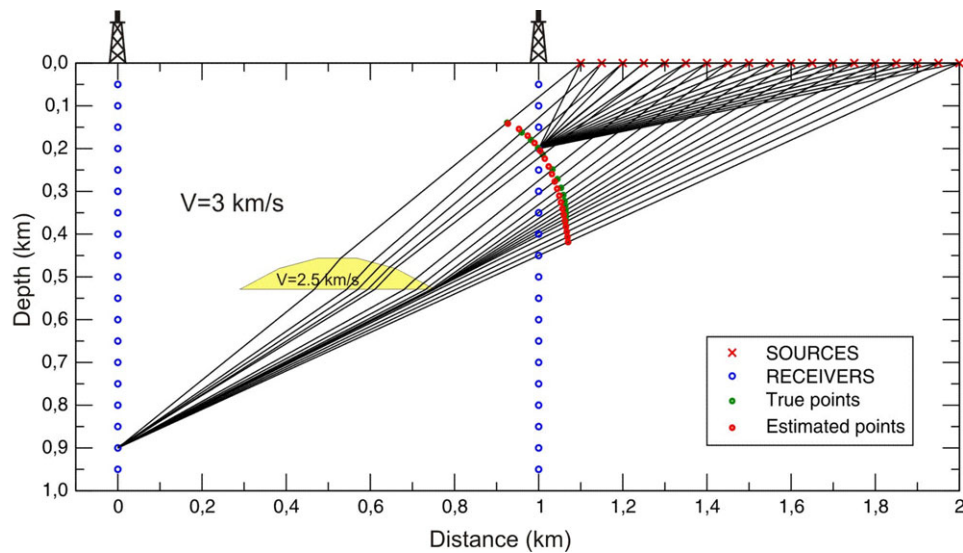


Figure 13 Application of the virtual method in the crosswell geometry. Stationary condition and projected points for a pair of receivers located in the two wells and sources at the surface.

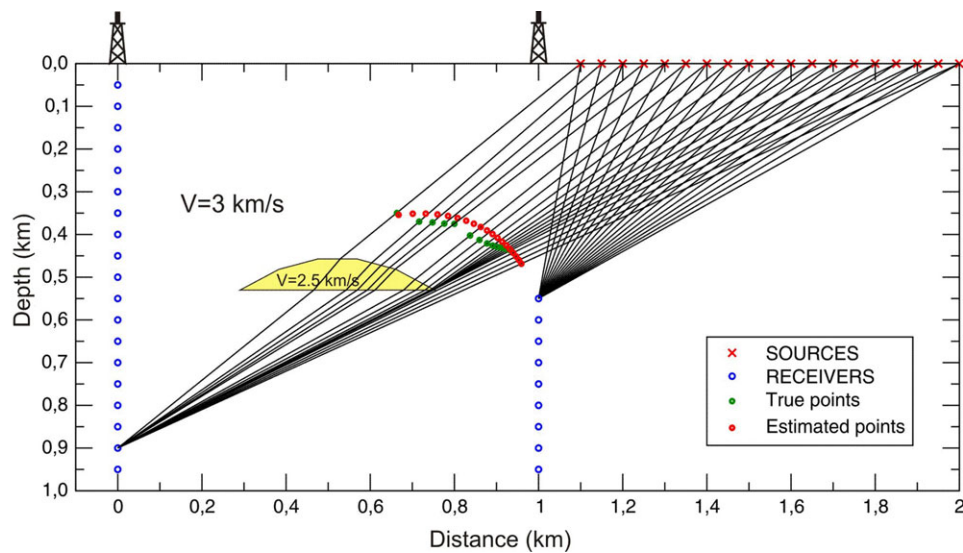


Figure 14 The same model of Fig. 13. Pair of receivers without stationary condition for conventional representation of virtual signals by direct arrivals.

30 Hz and 90 Hz, respectively. The signals in A and B were cross-correlated for each source position. Figure 6 shows the cross-correlations calculated for the complete circle. Then we picked the delay in the cross-correlated traces between the two signals recorded at the receivers A and B, and computed the corresponding tangent angle α . An example of a tangent line and an angle calculated with the source at the reference position 260° is shown in Fig. 6.

We estimated the location of the projected points P (denoted by yellow bullets in Fig. 5) for each source in the selected

source-angle range from 225° and 315° by a minimization of ray-tracing travel times. The estimated points are in agreement with the analytical ones. Figure 7 shows an example of cross-correlated traces (a) before and (b) after correction for the tangent of the source, which in this case is located at angle 260° . Figure 8 compares the similar TPI and conventional-interferometry Fresnel zones calculated in the first-order approximation for the source at angle 260° . It can be shown that minor differences in the tangent angles, of the order of few degrees, which can be due to small picking errors and

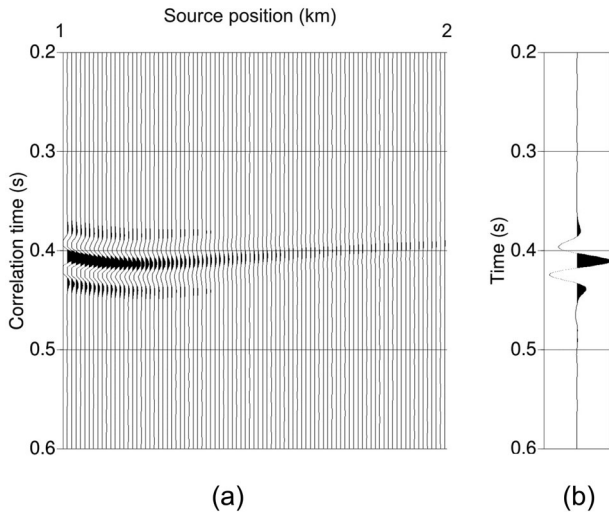


Figure 15 (a) Cross-correlations before stacking and (b) virtual-signal trace after stacking by conventional SI for the case of Fig. 13. In (a), the cross-correlations are calculated between receivers at depths of 0.2 km and 0.9 km in the wells of Fig. 13, using surface sources spaced every 10 m from 1 to 2 km source position in Fig. 13.

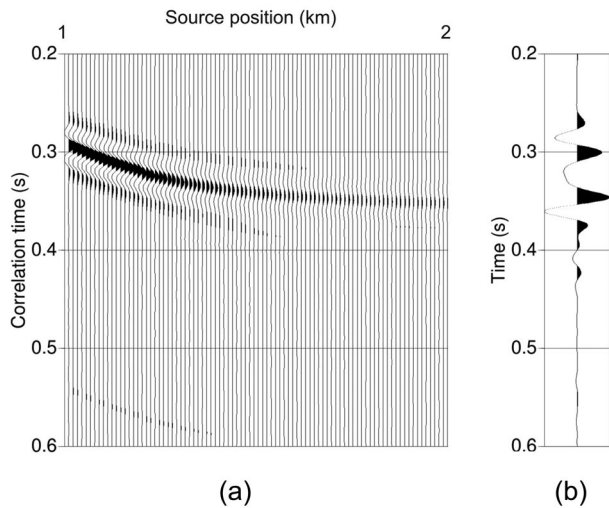


Figure 16 (a) Cross-correlations before stacking and (b) stacked signal obtained without stationary conditions in the case of Fig. 14. In (a) the cross-correlations are calculated between receivers at depths of 0.55 km and 0.9 km in the wells of Fig. 14, using surface sources spaced every 5 m from 1 to 2 km source position in Fig. 14.

phase variations in the modelled wavefields, can be considered second-order variations, which do not influence significantly the tangent-phase correction, which is zero by construction at the position of the source X_0 under correction.

The correction of the correlation gather is repeated for all the sources of the given interval. Summation of the corrected

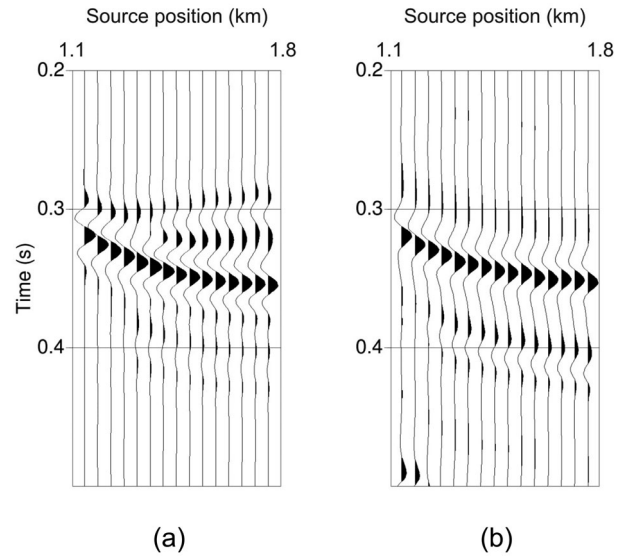


Figure 17 (a) TPI signal and (b) comparison with the corresponding synthetic signals from sources at the calculated projected points for the geometry of case of Fig. 14. The trace gathers are displayed showing traces obtained at selected source positions spaced every 50 m offset.

gathers provides the set of the TPI traces. Figures 9a and 9b show the TPI interferometry signal and the synthetic signals computed at the corresponding projected points, for result comparison. The coherent noise present between 0.2 s and 0.4 s in Fig. 9a is an artifact due to the periodicity in the cross-correlations; this is because the TPI data are not tapered before summation.

3.2 Phase distortions and signal tapering

We observe that the TPI interferometric signals are obtained by integration along paths of cross-correlated signal with variable curvatures, e.g., passing from upward concavity zone (at direct-positive correlation times) to a slanted flex—when the projected point reaches B—and then to a downward concavity zone (at reciprocal-negative correlation times) as in Fig. 6. When the data are not tapered before summation, the interference of signals with different waveforms caused by the curvature zones (Poletto *et al.* 2012a) may cause phase distortions. In conventional interferometry, the stationary zones are typically separated. To account for the variations in the phase of the interferometric signals due to curvature interference after tangent correction, signal tapering before correlation summation is beneficial. Including tapering for the cross-correlations

of selected events, equation (14) can be rewritten as

$$G(B, P, \omega) \cong (i\omega/V) \int_{S_0} \mathcal{T}(X, X_0) G(B, X, \omega) G^*(A, X, \omega) e^{-i\omega \tan(\alpha_0)(X-X_0)} dS, \quad (15)$$

where $\mathcal{T}(X, X_0)$ is a suitable space-tapering operator. Figure 10a, b shows a detail of Fig. 9, where the scaled time derivative is included to compensate for the dipole character in the TPI signal. Data are processed by moderate tapering, not relevant in the selected window of this figure. The agreement of the interferometry result and of the expected synthetic signal is good. We remark that an improved analysis of the phase distortion given by curvature variations should include the analysis of suitable optimal TPI tapering before summation, together with gating of selected events before correlation, which is not done at this stage of analysis.

3.3 Mapping projected points (non-uniform medium)

The data-driven TPI representation (equation 14) does not need model information. However, partial-model information is required in order to map the corresponding virtual-receiver points P . The analysis is performed considering that they are located on the wavefronts passing in A. In other words, to estimate the position of the projected points, we need to know the model from the sources to the projected points. This issue poses the problem to evaluate the sensitivity of the method to velocity. An iterative approach with travel-time tomography enables us to upgrade the model. We compare the computed (β) and the observed (α) angles (e.g., Lambaré *et al.* 2008) calculated by equations (8) and (9) to verify the tomography results. To calculate the tomographic inversion, we use an algorithm based on the simultaneous iterative reconstruction technique (Gilbert 1972). We discuss the case of a non-uniform model. In this analysis it is not necessary to know the entire travel paths from the real sources to B, and we assume that part of the velocity model is unknown. The corresponding wavefields propagating in the unknown area, from the projected points to B, are obtained by data-driven generalized-phase interferometry.

We analyze a model geometry similar to that of the first example, but with a non-uniform medium obtained by inserting a velocity function with a vertical gradient. The velocity ranges between 1 km/s at the bottom and 4 km/s at the top of the model. Figure 11a shows the bending rays calculated in the same source interval used for the uniform model. Red dots represent the source points, and the green dots represent the corresponding projected points. Figure 11b shows a detail of

the projected-point region shown in Fig. 11a, with the characteristic shape of the projection curves in this geometry. The estimation of the projected-point position is obtained using the local velocity model, together with wavefront constraints. We impose that the projected virtual receiver points are located on wavefronts passing through the receiver in A. The wavefront where to position the projected point for a given source on S includes those points at the constant propagation time (or phase by Eq. 3) equal to the traveltime (or phase) from said source to A. We adopt the solution to use a fictitious target approach to calculate the wavefront. We use a ray tracing algorithm (Böhm *et al.* 1999) to draw the rays from each source to a set of fictitious receivers placed beyond the expected wavefront passing in the receiver in A. To determine the constant-travel-time front on these rays, we need to know the local velocity model (Fig. 12). Note that here we use the fictional receivers only for the purpose to calculate the wavefront where to position the projected points (another approach could be the shooting method). The fictional receivers are not located on the wavefront, and they are not used in the subsequent analysis in which the projected points are positioned on the wavefront.

The projected point is at the intersection of the wavefront and the ray from the source to B (Fig. 12). Since part of the model after the wavefront is assumed unknown, the position of the projected point on the wavefront is tuned by tangent angle information and analysis of travel times. Rays are composed by parts drawn in the known- and unknown-model zones. We compute ray solutions by minimizing travel times of the ray paths, for each intersection between rays and wavefront. Local tomography inversion by an iterative approach is used to tune the model comparing the measured and calculated values. The first step of the iterative process starts from a uniform model in the unknown part, i.e., by straight rays in the unknown-model region (Fig. 12). The results are compared in Fig. 11b with that of the uniform medium of Section 3.1.

4 APPLICATIONS FOR SEISMIC EXPLORATION

We present applications of the tangent-phase interferometry using models with crosswell geometry, to illustrate its advantages for seismic exploration purposes. First we describe the results of TPI relative to conventional interferometry in a simpler model with a low-velocity lens. We show that TPI provides extended coverage for interferometry representation in the interwell region by direct events where the conventional approach can not be applied with the assumed recording

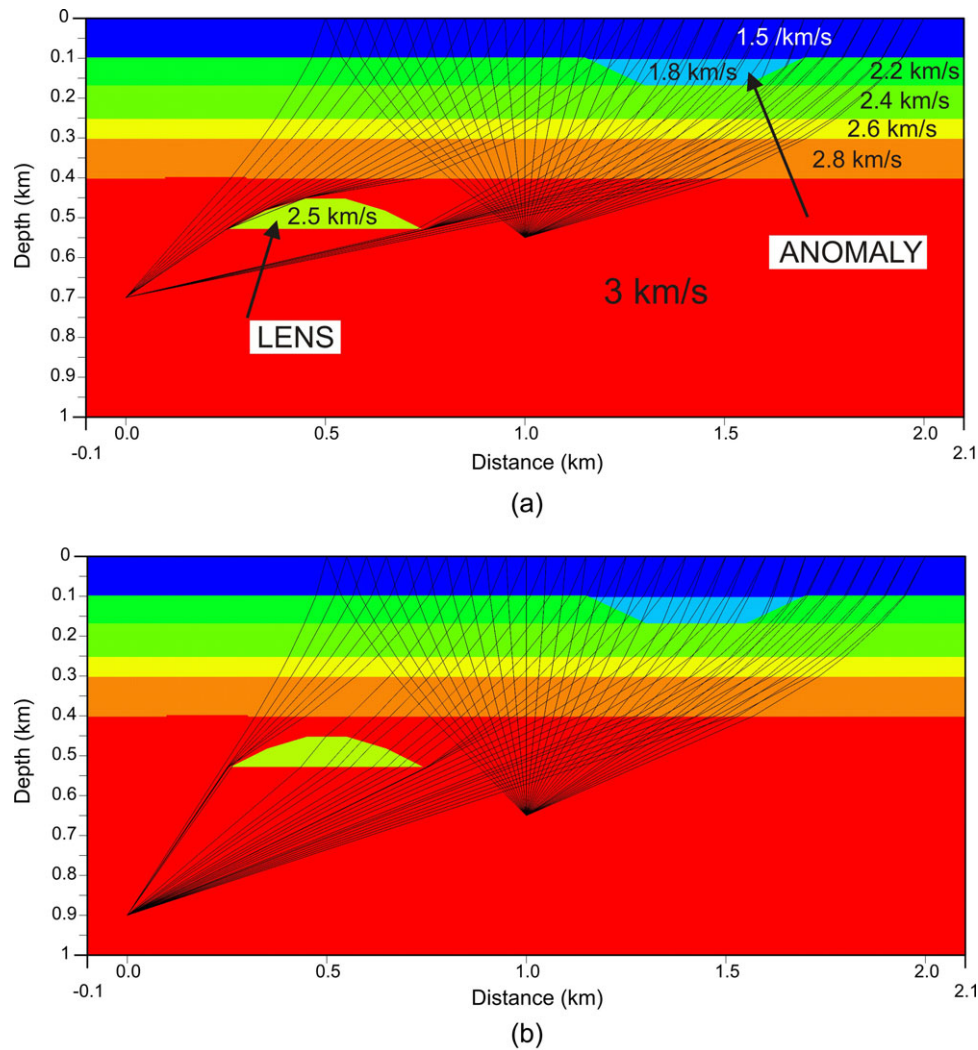


Figure 18 Layered crosswell model with the low-velocity lens and a shallow velocity anomaly. (a) Ray tracing showing non stationary geometry for conventional interferometry by the direct signals of a shallower recording receiver at 0.7 km in the left well, and of the reference receiver at 0.55 km in the right well; (b) Ray tracing showing non-stationary geometry for conventional interferometry by the direct signals of a deeper recording receiver at 0.9 km in the left well and of the reference receiver at 0.65 km in the right well.

geometry. Second, we discuss the possible limitations and issues for TPI in a more complex layered model, including a shallow velocity anomaly. This simulates uncertainties inside the region assumed as known.

4.1 Simple crosswell model with low-velocity lens

A numerical experiment is designed to compare complete and partial illumination conditions for stationarity in the crosswell geometry (Mehta *et al.* 2010). The model is shown in Fig. 13. The experiment consists of a set of geophones located inside two wells of 1 km depth, spaced with interwell distance of 1 km, and a shot line at the surface, extended

laterally for 1 km with respect to the two wells as shown in the figure. In this way we simulate different cones of illumination by direct arrivals from the surface sources with rays pointing to the buried receivers in the wells. The background medium velocity is 3 km/s. The model includes a half-lens low-velocity anomaly (2.5 km/s) inside the homogeneous velocity field. We take into account the interest for possible time-lapse variations.

Figures 13 and 14 show two different geometries of illumination for receivers in the well located at position 1 km in the model (reference well). In this well the receivers record the reference signals used for the interferometry representation. In Fig. 13, the illumination cone of the reference receiver selected

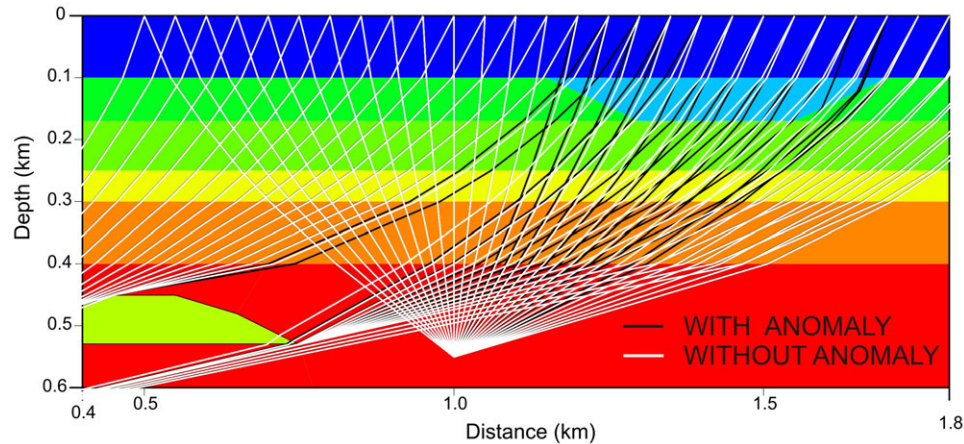


Figure 19 Comparison of the ray tracing obtained with (black lines) and without shallow anomaly (white lines) for the shallower pair of receivers at 0.7 km and 0.55 km.

at a depth of 0.2 km is contained in the cone of the receiver at a depth of 0.9 km in the well at lateral position of 0 m. The choice of this pair of receivers corresponds to a stationary condition for the conventional interferometry representation. When only a part of the receivers is available in the reference well, stationarity may not be satisfied in the conventional sense, as in Fig. 14. In this case, the shallower receiver is at a depth of 0.55 km, and its cone is not contained in that of the receiver at a depth of 0.9 km in the well at the position of 0 m (receiver well). This geometrical condition corresponds to lack of stationarity in the conventional sense. The cross-correlations (a) and summed signals (b) in the conventional interferometry representation are displayed in Figs. 15 and 16 for the cases of Figs. 13 and 14, respectively. It is evident the convergence in the first (Fig. 15b) and the non-convergence in the second case (Fig. 16b) for the interferometry direct arrival at approximately 0.4 seconds. To extend the stationarity zone for the direct arrival, we apply the TPI method. The projected point estimates (red dots) are calculated both for the stationary (Fig. 13) and the non-stationary conditions (Fig. 14). Figure 17a, b shows the comparison of the TPI signals with the synthetic ones computed from sources at the calculated projected points for the case of Figs. 14. We may observe in Fig. 17a, at approximately 0.3 seconds, some spurious event with an opposite slope trend with respect to that of the TPI signal. These artefacts are interpreted as acausal events due to cross-correlation contributions coming from the arrivals different from the direct signals, and to side-edge effects in the partial stack over the finite spatial window of the sources used in the integral representation.

4.2 Layered crosswell model with shallow velocity anomaly

We insert velocity variations with layers in the upper part of the model and, in addition, a shallow velocity-anomaly perturbation. In Fig. 18a, arrows indicate the low-velocity lens in the crosswell region and the shallow velocity anomaly. In this model, we draw the direct rays from the surface sources to the receivers in the left receiver well and to those of the right reference well. The wells are not shown in figure in order to obtain a clearer representation of the rays for a subset of sources. We selected two examples, one shallower and one deeper, which both have non-stationary conditions in the conventional sense. In Fig. 18a the receiver in the reference well is at a depth of 0.55 km. The receiver in the receiver well is at a depth of 0.7 km. The fan of the direct rays to the receiver at 0.7 km splits around the low-velocity lens. In Fig. 18b, the receiver in the reference well is at a depth of 0.65 km, and that in the receiver well is at a depth of 0.9 km. Part of the direct rays to the receiver at 0.9 km passes through the low-velocity lens.

With the purpose to evidence travelpath variations, Figure 19 illustrates a detail with the comparison of the direct rays to the receiver pair at 0.7 and 0.55 km in the models calculated with (black rays) and without (white rays) the shallow anomaly. There are some differences in the rays from the sources to the receivers, also due to the fact that the receivers are at relatively shallow positions. Due to the curvature of the rays, the near-surface paths from the sources at larger distances are similar for the receivers of the reference well and of the receiver well (note that here we compare rays with the same color). The near-vertical shallower

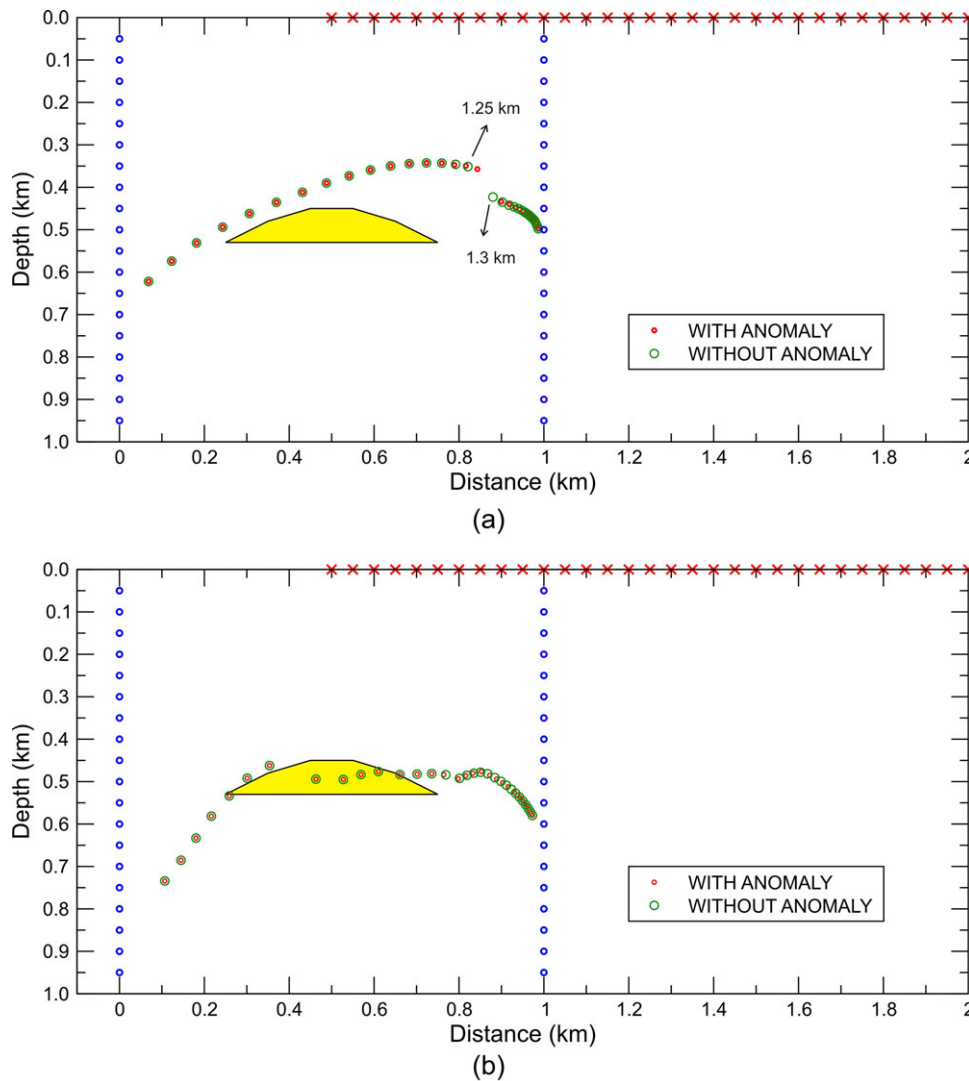


Figure 20 (a) Comparison of projected points calculated for the receivers at 0.7 km and 0.55 km, with (small red circles) and without (big green circles) the shallow anomaly. The arrows indicate the points for $X_0 = 1.25$ and $X_0 = 1.3$ km in the model without anomaly. (b) Comparison of projected points calculated for the receivers at 0.9 and 0.65 km, with (small red circles) and without (big green circles) the shallow anomaly. The shallower layers are omitted for clarity.

paths are removed with good approximation by signal cross-correlation. Also the shallow anomaly effect is removed with acceptable approximation for rays of the same receiver (in this case we compare rays with different colors). It can be shown that, for deeper receivers, as that at 0.9 km in the receiver well, the difference due to the anomaly becomes more negligible.

The presence of the shallow anomaly causes variations in the positions of the projected points. The projected points for the shallower receiver pair at 0.7 and 0.55 km are mapped in Figure 20a. The small circles represent the projected points

calculated with the anomaly for the sources marked at the surface. The big circles are the projected points calculated without the anomaly for the same sources. There are differences in the positions of the points calculated with and without the anomaly. The gap between circles corresponds to the split of the rays not passing through the low-velocity lens (see Fig. 18a). Figure 20b shows the projected points for the deeper receiver pair at 0.9 and 0.65 km. For this relatively deeper position, the ray verticality increases, and there is a good correspondence in the positions of the points calculated with and without the anomaly (see also Fig. 18b).

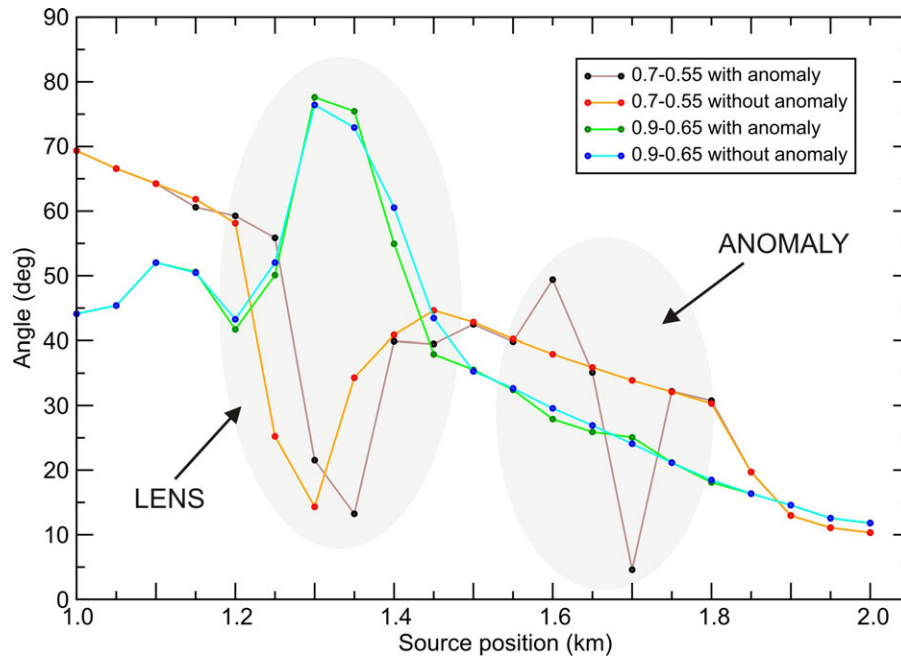


Figure 21 Spatial tangent angles β calculated for the points of Fig. 20a, b with and without shallow anomaly. The effect of the anomaly is irrelevant for the deeper receiver pair at 0.9 km and 0.65 km, in comparison to that for the shallower receiver pair.

As a consequence of the variation in the projected points, there is a variation in the corresponding spatial tangent angles. Figure 21 compares the expected effects induced by the shallow anomaly for the projected points calculated using the perturbed model. These results are calculated using the true-model information. The figure shows the angles β of the projected points in the models with and without the anomaly for the shallower receiver pair at 0.7 and 0.55 km, and for the deeper receiver pair at 0.9 and 0.65 km. For the shallower pair (at 0.7 km–0.55 km), the difference between the curves is relevant in correspondence with the source points affected by the anomaly. For the second pair (at 0.9 km–0.65 km), the difference between the curves is smaller and less relevant for TPI.

As discussed in previous sections, the tangent angles provide information useful to verify the model and the mapping of the projected points. The angles are analyzed in the model and data domains. Figure 22a shows $\tan \alpha$ calculated by β and V (equation 9) compared with the “true” values derived from travel times of ray tracing in the model without anomaly. The agreement is good, even if some instability is observed at source position 1.25 km where the rays split around the lens (Fig. 18a). The corresponding result calculated in the data domain (Fig. 22b) contains the effects of the Fresnel zone, which smooth the variation at approximately 1.25 km in Figure 22a for the presence of the low-velocity lens (see Figs. 18a and

20a). In Figure 22b, we observe the effects induced by the shallow anomaly in the time picking of the cross-correlated data. Tangent coefficients are measured by picking the direct arrivals in the cross-correlations of the signals of the pair at 0.7 and 0.55 km, simulated without and with the shallow anomaly. The result obtained with the anomaly presents a significant variation with respect to that obtained without the anomaly. The presence of this rapid and relevant tangent variation at approximately 1.5-km source position causes local distortions in the corresponding TPI representation. It can be shown that the tangents of the deeper pair of receivers at 0.9 and 0.65 km present smaller differences in the models with and without anomaly.

To evidence the variations and approximations induced in the TPI signals of the complex models, in the following figures we compare the signal raw cross-correlations, the TPI results and the signals of the synthetic projected-point signals (i.e., those calculated knowing the model) for different, shallower and deeper, receiver positions, with and without the shallow anomaly. We point out distortions and different effects due to the presence of the anomaly and to the presence of the low velocity lens (i.e., the lens already present in the previous model). Figure 23a, b shows the signals of the receiver pair at 0.7 and 0.55 km calculated without the anomaly. This figure compares (a) raw cross-correlations, (b) TPI, and (c) corresponding projected synthetic signals.

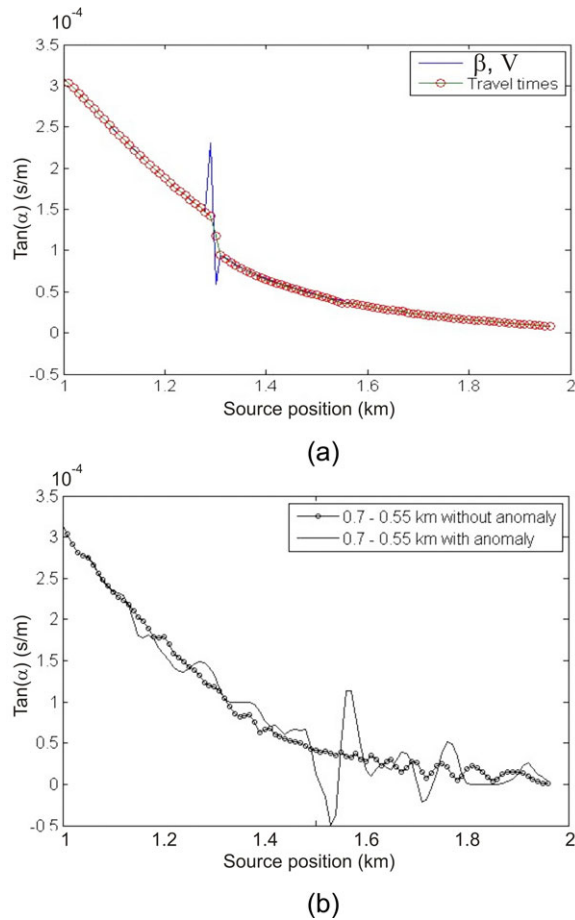


Figure 22 Apparent slope $\tan \alpha$ (ratio of the cross-correlation time increment relative to source position increment) for the receiver pair at 0.7 and 0.55 km. (a) Angles used in the analysis of the projected points. Comparison of tangent coefficients calculated using β and the local velocity V (blue line), and ray tracing travel times (green line with circle markers) in the model without anomaly. (b) Angles used to calculate the TPI signals. Comparison of tangent coefficients calculated by picking the cross-correlations of the synthetic signals of the receiver in the models with (simple line) and without (line with circles) the shallow anomaly. The tangent is calculated over five adjacent points.

Arrows indicate the edge effects induced by the low-velocity lens.

Figure 23c, d shows the corresponding signals of the receiver pair at 0.7 km and 0.55 km calculated with the anomaly. Arrows indicate the edge effects induced by the low-velocity lens and by the shallow anomaly. In the interpretation, we take into account the fact that the shallow anomaly induces a variation in the position of the projected points represented in the source domain (a similar effect can be observed also in Figure 20). The distortions in the TPI signal are interpreted as the effect due to the first-order tangent-phase

correction in the TPI representation in zones of rapid variations of the cross-correlation tangent. In this example, the tangent is calculated using the picked times of five adjacent shot points.

For comparison, Figure 24 shows the signals of the receiver pair at 0.9 km and 0.65 km calculated with the anomaly. In this case, because of the deeper position of receivers, the distortion effect of the anomaly is negligible.

5 DISCUSSION

Conventional interferometry can be in principle considered an exact representation for the Green's function recovery between receivers at known points, in which the correct wavefield estimate requires the knowledge of the local angle and velocity in the dipole character of the signal. This may pose the problem of making different estimations for different events in the represented trace (Wapenaar and Fokkema, 2006).

In the generalized-phase interferometry by TPI, the recovery of the waveform is performed for selected events, rather than for the entire trace. This can be regarded as a disadvantage of the TPI method. On the other hand, as an advantage, the approach provides for each pair of receivers a redundancy with a set of many traces at new projected positions, to be estimated by partial model knowledge. Moreover, this process can be repeated for several different events, providing other selected virtual signals with different projected locations. Iterative tomographic inversion is involved in this process of remapping selected events. The adapted inversion approach (Böhm *et al.* 1999; Poletto *et al.* 2012) exploits the time differences in the cross-correlation data before stacking, using the tangent condition together with, substantially, the information of the dual-difference tomography (Zhang and Thurber 2003). Correlogram-space analysis before data summation is used by Poliannikov and Willis (2011) to obtain improved virtual shot gathers in the conventional interferometry representation. In comparison, the TPI approach is focused on the signal representation by reconstruction of the Fresnel zone after tangent-phase correction and estimation of corresponding virtual sources.

The representation of the TPI events in zones of non-stationarity in the conventional sense appears to be robust using cross-correlation analysis and shift, supported by partial model information. This helps to determine and correct also the average dipole character of the signal. In a first approximation, the approach is robust with respect to the possible variations and errors in the location of the projection points where to attribute the virtual signals and estimate the

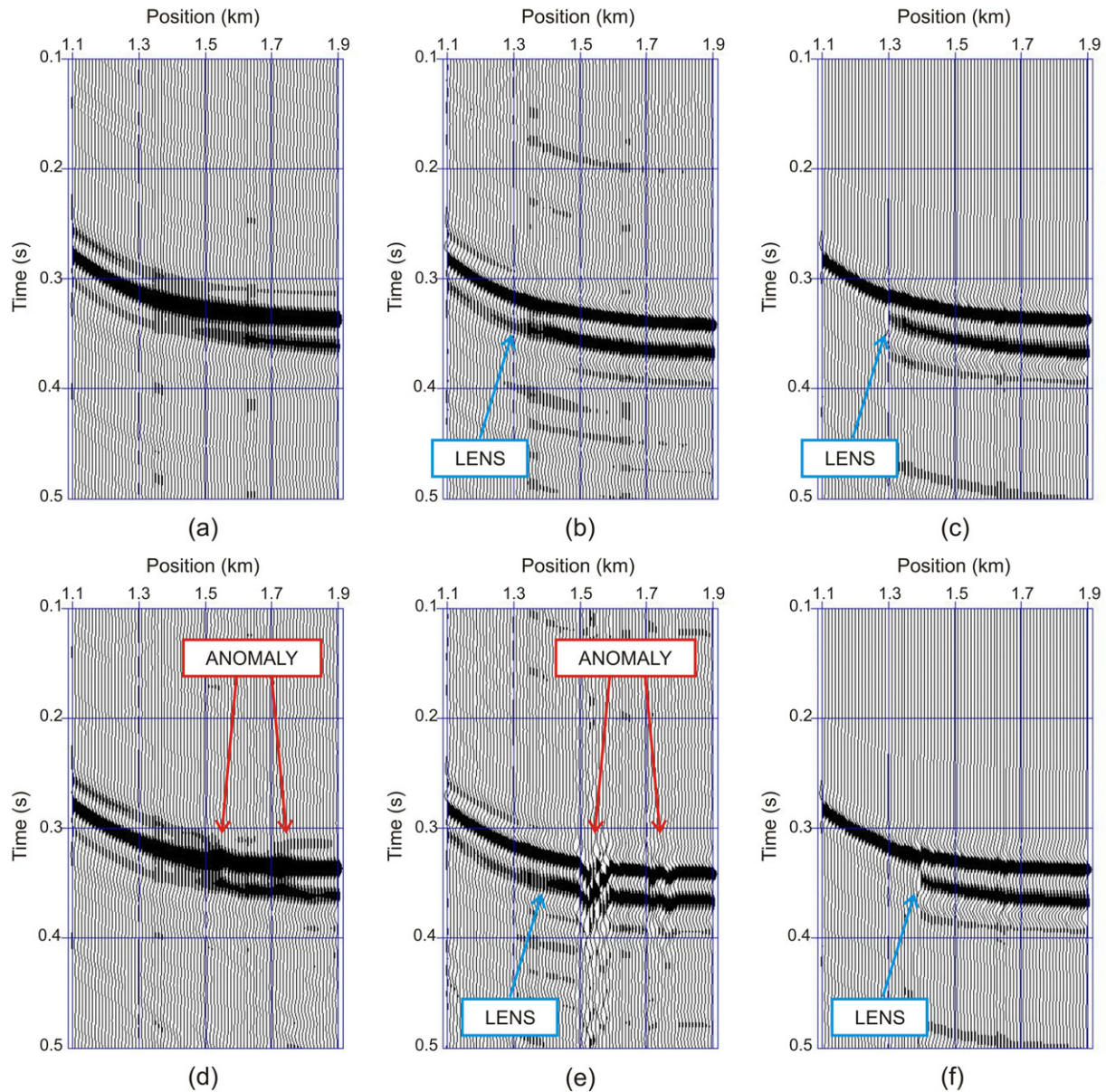


Figure 23 Model without the shallow anomaly. Signals of the receiver pair at 0.7 km and 0.55 km calculated in the source position interval from 1.1 to 1.9 km. (a) Cross-correlations, (b) TPI signals, and (c) signals of the corresponding projected points. The corresponding results in the model with the shallow anomaly are shown in (d), (e) and (f), respectively.

partial travel paths. From a computational point of view, the cost of the TPI signal is indicatively that of the conventional interferometry, multiplied by the number of source points for which the tangent-phase correction is calculated. For the projected points, the cost is determined by ray tracing, which depends on the model parameters. For the examples of this paper, the cost of ray-tracing is a few minutes. In experiments with larger datasets, it can be heavier.

Hence, time lapse using the reconstructed waveforms is envisaged as a possible advantageous application of this method where the conventional one fails for lack of coverage. A time-lapse application of generalized-phase interferometry is discussed by Poletto, Farina and Böhm (2013a), with analysis of sensitivity to velocity variations in the crosswell geometry. Diffraction analysis compared with TPI by direct arrivals shows that, in the presence of diffraction, reflection,

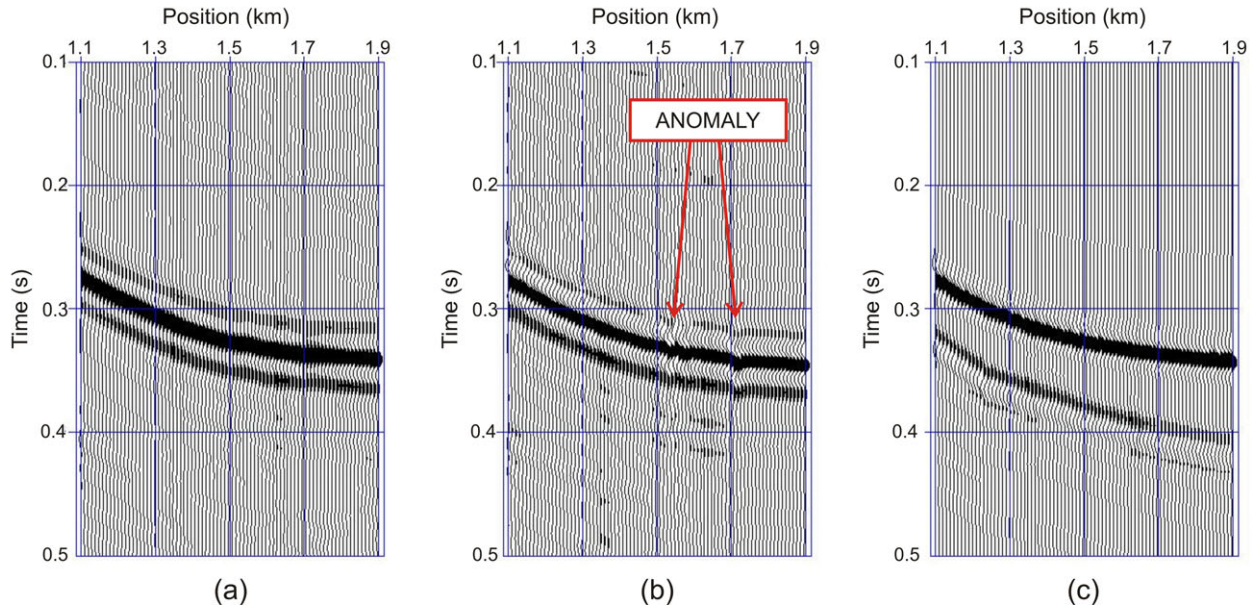


Figure 24 Model with the shallow anomaly. Signals of the receiver pair at 0.9 km and 0.65 km calculated in the source position interval from 1.1 to 1.9 km. (a) Cross-correlations, (b) TPI signals, and (c) signals of the corresponding projected points.

or multiple events, TPI requires separated corrections. The influence of random and coherent noise on accuracy of the method is an important aspect to be considered, in particular for the estimation of the tangent. Coherent noise can include reverberations and/or additional noise. It is envisaged that signal gating, or deconvolution, before cross-correlation, may be beneficial. In suitable cases with conflicting dips, the method makes it possible to separate upgoing and downgoing wavefields in the virtual signal reconstruction (Poletto *et al.* 2013b).

6 CONCLUSIONS

The generalized-phase interferometry method presented in this paper is a method to reconstruct virtual signals in cases where conventional seismic interferometry could fail because of poor coverage by real sources. The approach needs a phase correction, provided by the tangent analysis in the cross-correlations of the same data used for seismic interferometry purposes. This is done for selected events. New signals are obtained at new stationary projected points, which are defined for each pair of a source and a receiver along the signal wavefronts referred to a reference receiver, i.e., the receiver of the signal selected as the reference for the cross-correlation with the signals of the other receivers. The signal representation does not need model information. To determine the new projection points, the method uses a

mixed process based on the analysis of the tangent conditions in the cross-correlated data and on a traveltime minimization procedure considering a partial knowledge of the velocity model. This method allows us to extend interferometry to seismic exploration data where conventional illumination coverage is not sufficient to obtain stationarity condition.

REFERENCES

- Bakulin A. and Calvert R. 2006. The virtual source method: theory and case study. *Geophysics* 71(4), SI139–SI150.
- Bleistein N. 1984. *Mathematical methods for wave phenomena*. Academic Press, Inc.
- Böhm G., Rossi G. and Vesnaver A. 1999. Minimum time ray-tracing for 3-D irregular grids. *Journal of Seismic Exploration* 8, 117–131.
- Curtis A. and Halliday D. 2010. Directional balancing for seismic and general wavefield interferometry. *Geophysics* 75(1), SA1–SA14.
- Gilbert P.F.C. 1972. An iterative method for three-dimensional reconstruction of an object from projections. *J. Theor. Biol.* 36, 105–117.
- Lambaré G., Herrmann P., Toure J.-P., Suaudeau E. and Lecerf D. 2008. Computation of kinematic attributes for pre-stack time migration. 78th SEG Conference and Exhibition, Extended Abstracts, 2402–2406.
- Mehta K., Kiyashchenko D., Jorgensen P., Lopez J., Ferrandis J. and Costello M. 2010. Virtual source method applied to crosswell and horizontal well geometries. *The Leading Edge* 29, 712–723.
- Miller D., Oristaglio M. and Beylkin G. 1987. A new slant on seismic imaging: migration and integral geometry. *Geophysics* 52(7), 943–964.

- Poletto F., Bellezza C., Wapenaar K. and Craglietto A. 2012a. Virtual signals combination phase analysis for 2D and 3D data representation (acoustic medium). *Geophysical Prospecting* **60**, 838–854.
- Poletto F., Farina B. and Böhm G. 2012b. Seismic interferometry using a generalized phase approach. 74th EAGE meeting, Expanded Abstracts.
- Poletto F., Farina B. and Böhm G. 2013a. Tangent-phase interferometry, time lapse application and sensitivity analysis. 75th EAGE Conference and Exhibition, London, U.K., Expanded Abstracts.
- Poletto F., Farina B. and Böhm G. 2013b. Diffraction analysis by tangent-phase interferometry. 83rd SEG Conference and Exhibition, Extended Abstracts, 4608–4612.
- Poliannikov O.V. and Malcolm A. 2011. Interferometric microseism localization using neighboring fracture. 81st SEG Conference and Exhibition, Extended Abstracts, 4263–4267.
- Poliannikov O.V. and Willis M. 2011. Interferometric correlogram-space analysis. *Geophysics* **76**(1), SA9–SA17.
- Schuster G.T. 2009. *Seismic Interferometry*. Cambridge University Press, U.K.
- Schuster G.T. and Zhou M. 2006. A theoretical overview of model-based and correlation based redatuming methods. *Geophysics* **71**(4), SI103–SI110.
- Snieder R. 2004. Extracting the Green's function from the correlation of coda waves: A derivation based on stationary phase. *Physical Review E*, 046610.
- Spetzler J. and Snieder R. 2004. The Fresnel volume and transmitted waves. *Geophysics* **69**(3), 653–663.
- Stoffa P.L. 1989. Tau-p, a plane wave approach to the analysis of seismic data. *Kluwer Academic Publisher*, Dordrecht, The Netherlands.
- Vinje V., Iversen E. and Gjoystdal H. 1993. Traveltime and amplitude estimation using wavefront construction. *Geophysics* **58**(4), 1157–1166.
- Wapenaar K., Draganov D. and Robertsson J. 2008. Seismic interferometry: History and present status. Society of Exploration Geophysics, Geophysics Reprint Series 26, ISBN 978-1-56080-150-4.
- Wapenaar K. and Fokkema J. 2006. Green's function representations for seismic interferometry. *Geophysics* **71**(4), SI33–SI46.
- Zhang H. and Thurber C.H. 2003. Double-difference tomography: the method and its application to the Hayward Fault, California. *Bulletin of the Seismological Society of America* **93**(5), 1875–1889.